DOI: 10.61782/fa.2023.1224

forum acusticum 2023

NUMERICAL ASPECTS OF THE CO-ROTATING VORTEX PAIR PROBLEM IN AEROACOUSTICS

Mihály Ádám Ulveczki[1*] **Péter Rucz**[1]
[1] Faculty of Electrical Engineering and Informatics, Dept. of Networked Systems and Services, Budapest University of Technology and Economics

ABSTRACT

The co-rotating vortex pair is a well-known test problem for validating aeroacoustic computational frameworks. Both the flow field and the radiated acoustic far-field can be determined analytically, which allows for the direct comparison of all associated quantities. However, in order to simulate the vortex pair using numerical methods, several approximations must be made. One problem is caused by the singular velocity field at the center of the potential vortex, which must be treated by desingularization that also affects the resulting source terms. Another challenge in finite element formulations is the handling of the unbounded domain, which needs to be artificially truncated.

In our paper, the numerical aspects of the vortex pair problem are examined. The effects of the necessary approximations including the desingularization of the vortex-core and discretization to different computational methods are investigated. A method relying on the direct integration of the source terms is compared to different finite element solution strategies. Convergence tests are carried out and discussed for formulations of Lighthill's equation and the perturbed convective wave equation in the frequency domain.

Keywords: *computational aeroacoustics, co-rotating vortex pair, finite element methods*

*__Corresponding author__: *ulveczkim@hit.bme.hu.*

1. INTRODUCTION

In the hybrid computational aeroacoustic (CAA) framework, which is the commonly applied technique for the numerical simulation of sound radiation by low Mach number, weakly coupled flows, the acoustical quantities are determined in a series of computational steps. First, an incompressible flow simulation is performed, from which a sound source field is computed making use of an aeroacoustic analogy. Then, the propagtion of sound waves emitted by the sources is computed. The mismatch of the length-scales of the flow and the acoustic fields necessitates different spatial discretizations for the flow and acoustical propagation domains, which also requires the interpolation of the sources from the flow mesh onto the acoustical mesh. As the procedure involves a number of subsequent numerical approximations, it is very useful to have a validation case, where the effect of each of the above steps can be assessed.

The co-rotating vortex pair is a common test case for aeroacoustic simulations. It is one of the few arrangements where both the flow field and the far field radiated sound pressure can be determined analytically. This also allows for comparing different solutions for calculating the radiated field, as it is shown later in this article. Thus, the vortex pair is an important case for validating a hybrid CAA implementation. Nevertheless, the treatment of potential vortices in a numerical simulation must involve a desingularization, which can lead to deviations from the analytical solution in the far field radiated pressure. The aim of this paper is to examine the effects of the parameters of the vortex pair on the achievable convergence to the analytical solution. A numerical convolution method is introduced and the effect of different discretization configurations are discussed and compared to each other. The convergence study also provides a reference result for test-

ing further computational techniques, such as the finite element method (FEM).

The simulation setup and the analytical solution are discussed first in Section 2, and then the desingularization approach is also considered there. Section 3 introduces the methods applied for attaining the aeroacoustic sources and the simulation of sound propagation. The convergence analysis of a numerical convolution method is presented in Section 4, highlighting the effects of the desingularization on the achievable accuracy compared to the analytical solution. A finite element case study is addressed in Section 5 and a comparison to the converged results of the numerical convolution is made. Finally, the paper is concluded by the brief summary of Section 6.

2. PROBLEM DEFINITION

2.1 Co-rotating vortex pair

The co-rotating vortex pair consists of two potential vortices. The vortices rotate counterclockwise with a given circulation Γ, which also causes the two vortices to move as a pair in a circular arc of radius r_0 with respect to the geometric centre of the model, also counterclockwise. The angular frequency of the rotation is $\Omega_0 = \Gamma/(4\pi r_0^2)$. At the time instance $t = 0$, the vortices are aligned with the x axis. This arrangement is shown in Fig. 1.

The far field radiated sound pressure p of the vortex pair is derived by the matched asymptotic expansion technique [1] and is found as:

$$p(r,\theta,t) = \frac{\rho_0 \Gamma^4}{64\pi^3 c_0^2 r_0^4} \Big[J_2(k_0 r)\sin(2\Omega_0 t - 2\theta) - Y_2(k_0 r)\cos(2\Omega_0 t - 2\theta) \Big], \quad (1)$$

where r and θ are the polar coordinates, ρ_0 is the equlibrium density of the fluid, $k_0 = 2\Omega_0/c_0$ is the wave number with c_0 denoting the speed of sound in the free field, and J_2 and Y_2 are Bessel functions of the first and second kind, respectively. Eqn. (1) specifies a quadrupole field, which is shown in Fig. 2 at a given time instance. For evaluating the numerical approaches presented in the sequel, the solutions are compared on a reference section which is aligned with the x axis and spans $\lambda \leq r \leq 8\lambda$, where $\lambda = \pi c_0/\Omega_0$ is the acoustical wavelength.

2.2 Desingularization

In a numerical framework the treatment of the potential vortex is problematic due to the infinite velocity at the vortex core. To mitigate this issue, the vortices must be desingularized. One commonly applied approximation is the Scully vortex model [2], which gives the velocity field (u, v) of a single vortex as:

$$u = \frac{\Gamma}{2\pi} \frac{-(y - y_0)}{(x - x_0)^2 + (y - y_0)^2 + r_c^2}$$
$$v = \frac{\Gamma}{2\pi} \frac{(x - x_0)}{(x - x_0)^2 + (y - y_0)^2 + r_c^2} \quad (2)$$

x_0 and y_0 are the coordinates of the center of the vortex, while the r_c is the core radius. If $r_c = 0$, we obtain the singular solution, where the velocity approaches infinity

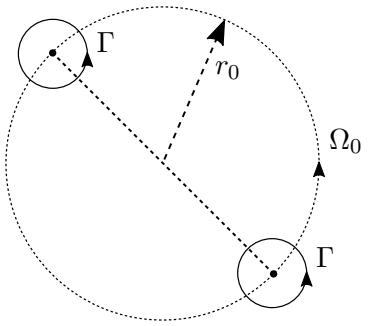

Figure 1. Arrangement of the co-rotating vortex pair

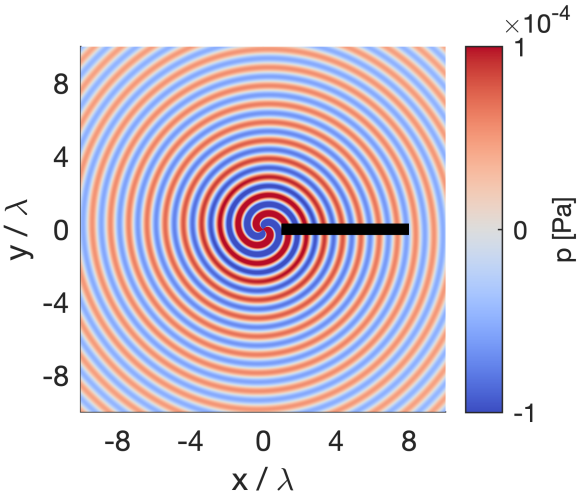

Figure 2. Analytical solution in a specific time and the evaluation line (black)

close to the center of the vortex.

Consider that when using the Scully model, the choice of r_c will exactly halve the velocity at $r = r_c$ distance. While the desinguarlization allows for the numerical treatment of the vortex pair problem in a CAA framework, it also affects the radiated sound pressure field, whilch will deviate from the analyical solution (1), as shown in the sequel.

3. METHODOLOGY

As discussed in the introduction, in hybrid CAA several steps need to be carried out for attaining the radiated acoustic field. Here, different approaches are addressed for extracting aeroacoustic sources from the incompressible flow field and computing their radiated sound pressure field.

3.1 Aeroacoustic sources

3.1.1 Lighthill's analogy

Lighthill's acoustic analogy [3] is written for the far field radiated sound pressure p as:

$$\frac{1}{c_0^2}\frac{\partial^2 p}{\partial t^2} - \nabla^2 p = \frac{\partial^2 T_{ij}}{\partial x_i \partial x_j} \qquad \text{(sum w.r.t. } i, j\text{)}, \tag{3}$$

where T_{ij} is the Lighthill tensor, which, in the case of low Mach numbers, can be calculated from the incompressible flow velocity field:

$$T_{ij} \approx \rho_0 u_i u_j. \tag{4}$$

It is useful to introduce the frequency domain version of Eqn. (3) with $p = \mathrm{Re}\left\{\hat{p}\mathrm{e}^{\mathrm{j}\Omega t}\right\}$ as

$$\nabla^2 \hat{p} + k^2 \hat{p} = -\frac{\partial^2 \hat{T}_{ij}}{\partial x_i \partial x_j}, \tag{5}$$

with $k = \Omega / c_0$ denoting the wave number.

3.1.2 Perturbed convective wave equation

The other wave equation considered here is the perturbed convective wave equation (PCWE) [4, 5], which is a reformulation of the APE-2 system of equations [6]:

$$\frac{1}{c_0^2}\frac{\mathrm{D}^2 \psi_a}{\mathrm{D}t^2} - \nabla^2 \psi_a = -\frac{1}{\rho_0 c_0^2}\frac{\mathrm{D}p_{\mathrm{ic}}}{\mathrm{D}t}, \tag{6}$$

where the acoustical velocity potential ψ_a was introduced using the definition $\mathbf{v}_a = -\nabla\psi_a$, with $\mathbf{v}_a$ denoting the acoustical particle velocity. In Eqn. (6) the total time derivative $\mathrm{D}/\mathrm{D}t = \partial/\partial t + \mathbf{v}\cdot\nabla$ is seen.

One advantage of the PCWE is that it can take the effect of mean flow in the propagation domain into account. The other difference compared to Eqn. (3) is that the formulation utilizes the pressure field of the incompressible simulation p_{ic} for the source terms.

3.2 Propagation

Here, we consider first a numerical convolution approach for computing the far field radiated pressure in the frequency domain. Moving to the frequency domain is justified by the fact that the convolution by the 2D Green's function is cumbersome in the time domain. Furthermore, the time-periodicity of the vortex pair problem makes the use of the frequency domain convenient.

The Green's function G is defined by the relation

$$\nabla^2 G(\mathbf{x}, \mathbf{x}_0) + k^2 G(\mathbf{x}, \mathbf{x}_0) = -\delta(\mathbf{x} - \mathbf{x}_0), \tag{7}$$

with δ denoting the Dirac delta distribution. If the Lighthill tensor is known in each point of the domain V, the sound pressure field is attained as a convolution:

$$\hat{p}(\mathbf{x}) = \int_V G(\mathbf{x}, \mathbf{x}_0)\frac{\partial^2 \hat{T}_{ij}(\mathbf{x}_0)}{\partial x_i \partial x_j}\,\mathrm{d}\mathbf{x}_0. \tag{8}$$

The derivatives on the right hand side can be rearranged to the Green's function by means of applying integration by parts twice. As the domain is unbounded in our case, the arising boundary terms vanish and the following result is found:

$$\hat{p}(\mathbf{x}) = \int_V \frac{\partial^2 G(\mathbf{x} - \mathbf{x}_0)}{\partial x_i \partial x_j}\hat{T}_{ij}(\mathbf{x}_0)\,\mathrm{d}\mathbf{x}_0. \tag{9}$$

Since the Green's function is a less abruptly changing function than the Lighthill tensor itself ($r_c, r_0 \ll \lambda$), shifting the derivative is expected to allow a less fine spatial discretization of V and hence a reduction of the computational effort.

The flow pressure field p_{ic} can also be used as source of the calculation, however, in this case the computation includes the total derivative. In the low Mach number limit, the simplification $\mathrm{D}/\mathrm{D}t \approx \partial/\partial t$ can be applied for the wave propagation, and making use of the Euler equation $\nabla\hat{p} = -\mathrm{j}\Omega\rho_0\mathbf{v}_a$, the sound pressure in the frequency domain is found as:

$$\hat{p}(x) = -\int_V G(\mathbf{x} - \mathbf{x}_0)\frac{\mathrm{j}\Omega}{c_0^2}\hat{q}(\mathbf{x}_0)\,\mathrm{d}\mathbf{x}_0, \tag{10}$$

where $\hat{q} = \mathcal{F}\{\mathrm{D}p_{\mathrm{ic}}/\mathrm{D}t\}$ is the frequency domain representation of the source term.

4. CONVERGENCE ANALYSIS

The convergence of the convolution integral strategy is tested in this section. The sole numerical approximation in this case is the discretized evaluation of the convolutions in Eqn. (8) and (9), where only the source region is discretized. Thus, possible errors due to the interpolation of the source terms, or numerical dispersion in the propogation domain are avoided. Hence, if a converged result is attained using this method, it can be used later as a reference solution to which FEM results can be compared.

The common parameters of the simulation cases are the following: circulation $\Gamma = 1.005321\,\mathrm{m}^2/\mathrm{s}$, angular frequency $\Omega_0 = 0.08\,\mathrm{rad/s}$, distance between origin and center of the vortex $r_0 = 1\,\mathrm{m}$, equilibrium density of the fluid $\rho_0 = 1\,\mathrm{kg/m}^3$. The core radius r_c, the speed of sound c_0 and the truncation radius R of the infinite domain V are varied in different tests.

4.1 Integration strategy

Making use of the periodic motion of the vortex pair, the periodicity of the source term q [with q denoting a general source term in Eqn. (8), (9), or (10)] is exploited, and the size of the integration domain can be significantly reduced. Integration over a circular area can then be performed by evaluating the source terms only over a slice of the domain $V_{\mathrm{sl}} : 0 \leq r \leq R, 0 \leq \theta \leq \pi/N_{\mathrm{sl}}$, where N_{sl} is the number of slices, taken conveniently as an integer power of 2. The total integration domain consists of $2N_{\mathrm{sl}}$ slices. Numbering these slices in the positive (counterclockwise) direction, we find for the n-th slice that

$$q^{(n)}\left(\mathbf{x}^{(n)}, t\right) = q^{(0)}\left(\mathbf{x}^{(0)}, t - \frac{\pi n}{\Omega_0 N_{\mathrm{sl}}}\right), \qquad (11)$$

where $\mathbf{x}^{(0)}$ is a spatial location in the first slice (i.e., the slice over which the actual convolution is performed), $\mathbf{x}^{(n)}$ is the same coordinate rotated by an angle of $n\pi/N_{\mathrm{sl}}$ around the origin. The upper indices in parentheses denote the number of the slice. The time delay $t_n = \pi n/(\Omega_0 N_{\mathrm{sl}})$, or an equivalent phase shift in the frequency domain, results from the angle and the angular velocity of the rotation of the vortex pair.

Finally, the slice V_{sl} is subdivided into integration subdomains, and the base points of a Gaussian quadrature in the polar coordinate system are used in each subdomain

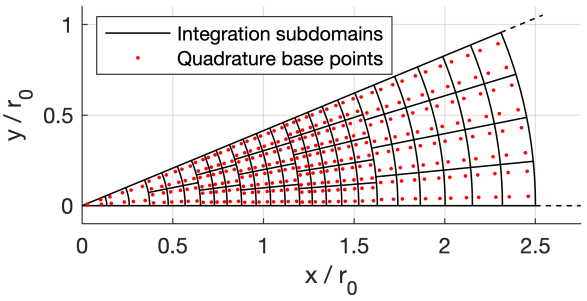

Figure 3. Numerical integration strategy

for the discretization of the convolution integral. As also illustrated in Fig. 3, the finest spatial resolution is applied in the region $r \approx r_0$.

4.2 Radiation by the spectral components

In the frequency domain, an interesting phenomenon can be discovered when examining the excitation and the pressure response. Fig. 4(a) shows the spectrum of the Lighthill source term in Eqn. (3) at the radius $r = 1.25r_0$. It can be seen that we have the spectrum of a smooth periodic, but non-harmonic function, since the first few components take on a non-zero value and a decay is observed as the frequency increases. However, as it is seen in Fig. 4(b) only the first component (angular frequency $2\Omega_0$) radiates into the far field, as also predicted by the analytical formula (1). While excitation by higher frequency components cancel out due to the geometrical symmetry, the presence of the higher components must not be neglected when a finite element formulation of the sound radiation is considered. The maximum allowable frequency for which the largest element size is still smaller than $\lambda/10$ is shown as the dashed vertical line in Fig. 4(a) for the FE mesh used later in this study. While in a frequency domain simulation the frequency content of the aeroacoustic source terms is easily controlled, the extended frequency bandwidth of the source has to be taken into account if the computation is performed in the time domain.

4.3 Convergence results

We first discuss the variation of the minimal spatial resolution required with different choices of the core radius r_c. In this case the fixed parameteres are: $R = 300r_0$, $c_0 = 8\,\mathrm{m/s}$, i.e., $\mathrm{Ma} = 0.01$. The effect of changing the size of the integration subdomains is shown in Fig. 5.

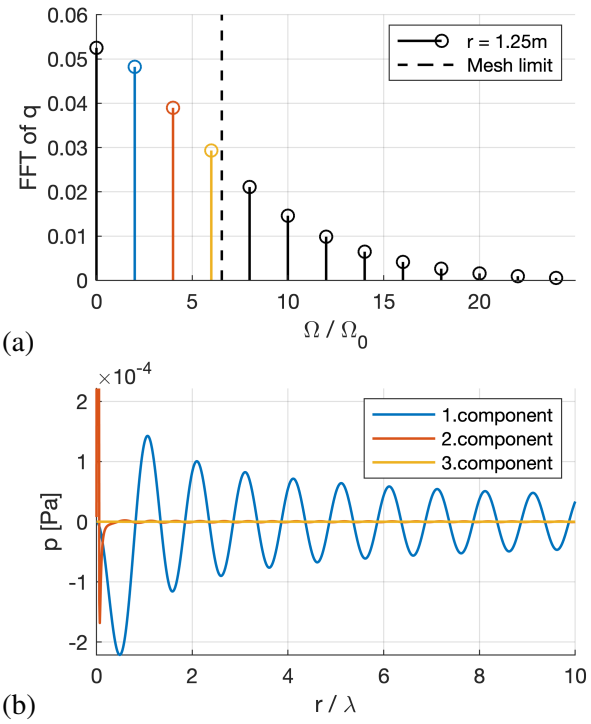

Figure 4. (a) Spectrum of the excitation source term (b) Sound pressure radiated by the first 3 harmonic components of the excitation

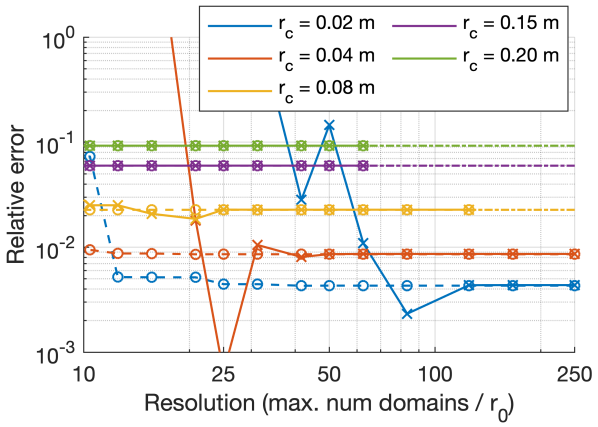

Figure 5. Effect of the element size and core radius on the results of the numerical convolution with different r_c values. Solid lines and "x" markers: Eqn. (8). Dashed lines and circle markers: Eqn. (9).

The dash-dotted curves are a continuation of the results, where convergence was already attained using smaller resolutions. Convergence was reached in all cases, and the two strategies of Eqn. (8) and (9) converge to the same relative error compared to the analytical solution.

The error caused by the core radius r_c is also interesting to observe in Fig. 5. As r_c increases, the error limit increases as well, from 0.4% ($r_c = 0.02\,\mathrm{m}$) to 9.6% ($r_c = 0.20\,\mathrm{m}$). On the other hand, it can also be observed that with increasing r_c convergence is achieved with lower spatial resolutions in all cases, as a result of the Scully vortex model smoothing out the steeper spatial variations of the Lighthill source term at higher r_c values. Shifting the spatial derivatives to the Green's function resulted in reaching convergence with 2.5 to 4 times smaller resolutions, which trend was expected as explained above.

The effect of changing the speed of sound c_0 and the truncation limit R is depicted in Fig. 6. Here, $r_c = 0.02\,\mathrm{m}$ is used, and the spatial resolution is chosen at the convergence limit observed above (125 domains $/r_0$). The figure shows the results of two methods in a similar way as Fig. 5. It can be seen that as the Mach number increases (i.e., c_0 decreases), the limit error increases gradually.

The effect of the truncation limit R on the results is also interesting to observe in Fig. 6. As the Mach number decreases, a higher R is required to arrive at the limit of convergence: while for $\mathrm{Ma} = 0.08$ the limit is near $R/r_0 = 30$, at $\mathrm{Ma} = 0.001$, $R/r_0 \approx 500$ is required to reach convergence. While the two methods converge to the same result, the shape of the curves for the truncation limit R is apparently completely different for the two methods. When the derivative is on the Lighthill tensor [Eqn. (8)], the curve approximates the converged value from above (i.e., the error decreases monotonically as R is increased), while in the case where the spatial derivatives are shifted to the Green's function [Eqn. (9)], we observe a sudden drop in the error as R is increased, and then the converged value is reached from below.

The implications of the results on the truncation limit are also worth discussing. First, the convergence limit tells the minimal size of the flow mesh that is necessary to achieve the minimal error. Second, it is noticed that the truncation size at the convergence limit becomes comparable to the wavelength, and the assumption of a compact source ($R \ll \lambda$) no longer holds if the whole source region is considered. While in case of singular potential vortices, the vortices represent point sources, the effective source size increases dramatically by the desingularization.

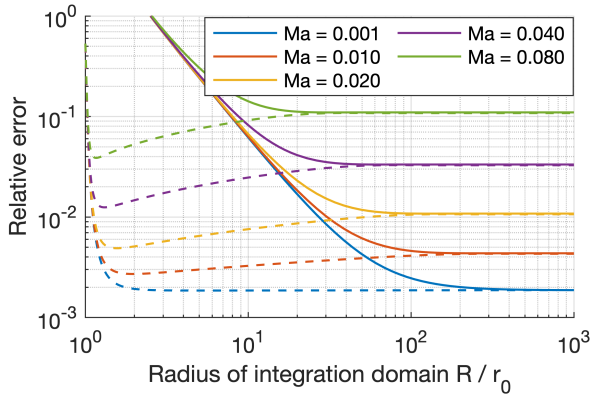

Figure 6. Effect of the truncation limit R at different Mach numbers Ma. Solid lines: Eqn. (8). Dashed lines: Eqn. (9).

Finally, it has to be highlighted that the final error has a similar shape in all converged cases: the phase of the radiated sound pressure matches exactly that of the analytical solution, while the magnitude is smaller than the analytical one by a constant factor, i.e., independent of the distance. The decrease of the magnitude is expected, since the desingularization (2) decreases the velocity. As the only approximation made here is the numerical evaluation of the convolution integral, the converged results can serve as a reference when more involved computations, such as the FEM, are considered.

5. FINITE ELEMENT SIMULATION

5.1 FE methodology

We consider first the Helmholtz equation with Lighthill sources, i.e., Eqn. (5). The Lighthill sources are approximated using the finite element shape functions $\phi_k(\mathbf{x})$ as

$$\hat{T}_{ij}(\mathbf{x}) \approx \sum_{k=1}^{n} \phi_k(\mathbf{x}) \hat{T}_{ijk}. \tag{12}$$

In the presented example, linear isogeometric elements are used. By applying the standard Galerkin method on the weak form, a spatial derivative is shifted from the Lighthill tensor onto the shape functions. The arising boundary term is cancelled anew [7]. For the PCWE source terms, we apply a similar approximation:

$$\hat{q}(\mathbf{x}) \approx \sum_{k=1}^{n} \phi_k(\mathbf{x}) \hat{q}_k. \tag{13}$$

Then, the standard Galerkin formulation is utilized.

The parameters for the reference case are chosen as $c_0 = 1\,\mathrm{m/s}$ ($\lambda = 39.3\,\mathrm{m}$) and $r_c = 0.1\,\mathrm{m}$, and the other parameters are the same as in Section 4. First, a flow mesh is generated, which has a rectangular shape. In the center $6 \times 6\,\mathrm{m}$ area of the mesh the element size is uniformly $l_{\min} = 0.02\,\mathrm{m}$, while away from the center, the size of the elements increases gradually up to $l_{\max} = 0.5\,\mathrm{m}$, at $r = 50\,\mathrm{m}$, which is half the edge length of the total flow domain. The velocity field and the Lighthill tensor field are evaluated on a fluid mesh using (2) and (4) and the latter is transformed into the frequency domain. In case of the PCWE, the method described in [8] is utilzed for computing p_{ic} from the velocity and complex flow potential fields.

The acoustical mesh also has a rectangular shape, and has a total size of $400 \times 400\,\mathrm{m}$, with the element sizes increasing gradually from 0.08 to $1.0\,\mathrm{m}$ towards the edge. For emulating free field radiation conditions, the PML formulation presented in [9] is utilized and a layer of $20\,\mathrm{m}$ thickness is attached to the propagation domain. Conservative interpolation [7, 10] is utilized for interpolating the discretized source terms from the flow mesh onto the acoustical mesh.

The matrix equation resulting from the discretization of the weak forms of the governing equations reads as

$$\left(\mathbf{K}_a + \mathrm{j}\Omega\mathbf{C}_a - \Omega^2\mathbf{M}_a\right)\mathbf{p} = \mathbf{A}_p\mathbf{f}_f, \tag{14}$$

where $\mathbf{K}_a$, $\mathbf{M}_a$, and $\mathbf{C}_a$ are the acoustical stiffness, mass, and damping matrices, $\mathbf{f}_f$ is the forcing vector on the flow mesh, resulting from the Lighthill or PCWE sources, and $\mathbf{A}_p$ is an auxiliary sparse matrix of the conservative interpolation. Eqn. (14) is solved for the pressure unknowns represented by the vector $\mathbf{p}$. The inverse Fourier transform can be applied for finding the pressure field at an arbitrary time instance in the steady state, as shown in Fig. 7. The quadrupole field is perfectly reproduced by the FEM, and no spurious reflections are observed from the PML interface. Overall, a very good agreement with the analytical solution is observed in both cases.

5.2 Evaluation of the differences between the simulation methods

It is worth noting again that we can only expect the model to approximate the converged integration result, since the FEM introduces new approximations in addition to the desingularization, which stem from several steps. Because the flow domain being already discretized (a flow

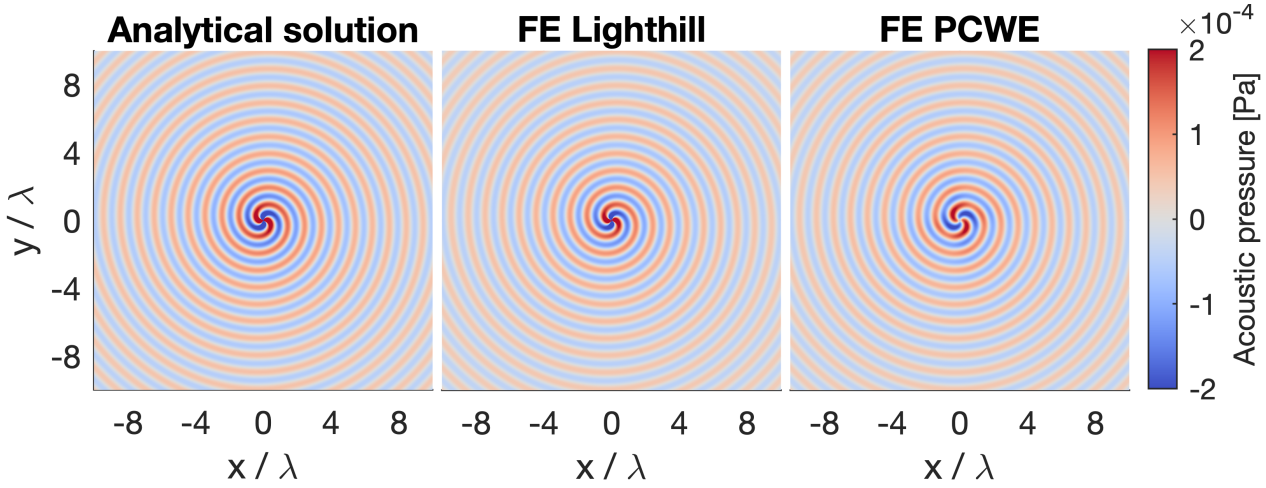

Figure 7. Comparision of analytical and FEM solutions in the whole simulation domain

mesh was used instead of the integration subdomains of the convolution), refining the acoustical mesh can only increase the accuracy up to a certain limit. The interpolation of the aeroacoustic source terms can also introduce an error. Contrary to the numerical convolution by the Green's function, the propagation phase is also subject to numerical dispersion in the FEM. Finally, an artificial truncation of the simulation domain is necessary for imitating free field radiation conditions.

With these considerations in mind, we can observe the error given by the methods in Fig. 8. In all cases, the error is evaluated on the black evaluation line shown previously in Fig. 2. While there are many possible sources of error in the FE solution, the final result only differs by a minimal extent from the converged convolution result (dotted curve in Fig. 8), which highlights that the error introduced by the desingularization is dominant. Similar to the cases discussed in Section 4, the magnitude of the analytical solution is underestimated by the FEM as well. It is also observed that the FEM results are almost perfectly aligned in phase with both the analytical and the converged numerical convolution results, showing that the chosen discretization does not introduce a significant numerical dispersion error.

While the near field is not visible Fig. 8, it is interesting to observe in Fig. 7, that in the near field of the vortex pair (for $r < \lambda/2$) remarkable differences are present between the Lighthill and PCWE FEM results. As both techniques as well as the analytical formula rely on the far

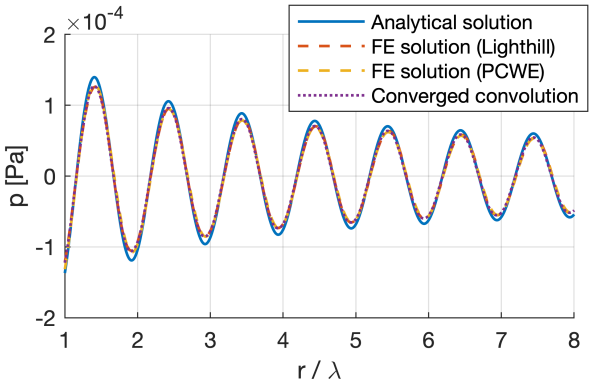

Figure 8. Comparision of different simulation methods on the same evaluation line

field approximation, the near field cannot be expected to be reproduced by neither methods, and it should be excluded from the evaluation of the relative error.

6. CONCLUSION

In this paper we dealt with one of the common validation arrangements in flow acoustics, the co-rotating vortex pair. The analytical solution for the far field radiated pressure was compared to numerical convolution of the source terms resulting from desingularized vortices by the Green's function in the frequency domain. The parame-

ters affecting the convergence of the computational procedure were examined and the minimal achievable errors were determined. By examining the effect of the truncation radius of the integration domain, it was found that the source region of the desingularized vortices can no longer be considered as compact. The latter result also explains the higher deviation from the analytical solution at slightly greater Mach numbers ($\mathrm{Ma} \approx 0.1$). Based on the convergence results of the convolution, a finite element test case was created and the results of the FE simulation were compared with both the analytical and converged numerical solutions using both Lighhill sources and the perturbed convective wave equation. Despite the fact that errors may stem from several steps of the finite element procedure, the FE solution approximated the converged numerical convolution very well. This study shows that a relatively simple validation problem like the vortex pair may already suffer from various sources of errors, which renders the reconsideration of validation cases worthwhile.

7. ACKNOWLEDGMENTS

Supported by the ÚNKP-22-3-II-BME-244 New National Excellence Program of the Ministry for Culture and Innovation from the source of the National Research, Development and Innovation Fund. This work has been supported by the Hungarian National Research, Development and Innovation Office under contract No. K–143436.

8. REFERENCES

[1] B. E. Mitchell, S. K. Lele, and P. Moin, "Direct computation of the sound from a compressible co-rotating vortex pair," *Journal of Fluid Mechancis*, vol. 285, pp. 181–202, 1995.

[2] M. P. Scully and J. P. Sullivan, "Helicopter rotor wake geometry and airloads and development of laser Doppler velocimeter for use in helicopter rotor wakes," tech. rep., Massachusetts Institute of Technology, Aerophysics Laboratory, 1972.

[3] M. J. Lighthill, "On sound generated aerodynamically. I. General theory," *Proceedings of the Royal Society of London*, vol. 211, no. 1107, pp. 564–587, 1952.

[4] M. Kaltenbacher and A. Hüppe, "Advanced finite element formulation for the convective wave equation," in *Proceedings of Euronoise 2018*, (Crete, Greece), pp. 291–295, 2018.

[5] S. Schoder, C. Junger, and M. Kaltenbacher, "Computational aeroacoustics of the EAA benchmark case of an axial fan," *Acta Acustica*, vol. 4, no. 5, p. 22, 2020.

[6] R. Ewert and W. Schröder, "Acoustic perturbation equations based on flow decomposition via source filtering," *Journal of Computational Physics*, vol. 188, pp. 365–398, 2003.

[7] M. Kaltenbacher, M. Escobar, S. Becker, and I. Ali, "Computational aeroacoustics based on Lighthill's acoustic analogy," in *Computational acoustics of noise propagation in fluids – Finite and boundary element methods* (S. Marburg and B. Nolte, eds.), ch. 4, pp. 115–142, Springer, 2008.

[8] C. Junger, *Computational aeroacoustics for the characterization of noise sources in rotating systems*. PhD thesis, Technical University of Vienna, 2019.

[9] B. Kaltenbacher, M. Kaltenbacher, and I. Sim, "A modified and stable version of a perfectly matched layer technique for the 3-D second order wave equation in time domain with an application to aeroacoustics," *Journal of Computational Physics*, vol. 235, pp. 407–422, 2013.

[10] S. Schoder, C. Junger, M. Weitz, and M. Kaltenbacher, *Conservative source term interpolation for hybrid aeroacoustic computations*, pp. AIAA 2019–2538.